# 16-Channel Directly Modulated Membrane III-V Laser Array on $SiO_2$/Si Utilizing Photon-Photon Resonance

Nikolaos-Panteleimon Diamantopoulos, *Senior Member, IEEE, Senior Member, Optica*, Takuro Fujii, *Member, IEEE*, Suguru Yamaoka, Hidetaka Nishi, *Member, Optica*, Koji Takeda, *Senior Member, IEEE*, Toru Segawa, *Member, IEEE*, and Shinji Matsuo, *Fellow, IEEE, Fellow, Optica*

*(Post-Deadline Paper)*

***Abstract*—Following the demand for 1.6 Tbps and beyond data rates and lower power consumption transceivers in data center networks and related systems, we present the first 16-channel directly modulated laser (DML) array exhibiting the photon-photon resonance (PPR) effect. Bandwidths of ∼50 GHz at bias currents between 6.1 ∼ 9.2 mA were achieved for all 16 channels in a membrane laser array on $SiO_2$/Si with optimized integrated optical feedback for stable PPR control, denoting a record bandwidth × no. channel product. The DML array has been demonstrated in an O-band short-reach link by using 100-GBaud NRZ modulations, resulting in <130 fJ/bit laser-operating energies. These results denote a significant stride towards ultra-low power consumption DML transmitters for 1.6 Tbps interconnects and beyond.**

***Index Terms*—Directly modulated lasers, heterogenous integration, optical interconnects, optical transceivers.**

## I. Introduction

As THE demand for higher data rates and lower power consumption in data center networks intensifies, fueled by the increased traffic from cloud and AI services [1], the industry is actively working to ensure sustained efficiency and scalability through the widespread adoption of optical interconnects that adhere to evolving Ethernet and related standardizations [2], [3]. Current projections anticipate near-future data rates of 1.6 Tbps and beyond, facilitated by multi-channel transceivers with symbol rates of 100 GBaud or more per channel [2]. To meet these challenges while simultaneously reducing device footprint, the adoption of increased integration density co-packaged optics (CPO) is underway [3].

Regarding integrated multi-channel transmitters (Tx), low-operating-power directly modulated lasers (DMLs) [4] and specifically membrane DMLs fabricated on Si substrates [5], [6], [7], [8], [9], [10], [11], [12], offer a very promising solution. These devices offer substantial bandwidth and energy efficiency in a very compact form factor due to the high optical confinement of the membrane structure. Meanwhile, their fabrication on Si substrates can leverage large-scale Si wafer manufacturing with mature CMOS-compatible processes.

By using arrays of such membrane DMLs we have previously demonstrated devices and systems capable of 400/800-Gbps utilizing either wavelength- or space-division multiplexing (WDM [6], [7] / SDM [8], [9]). Moreover, very recently we have also demonstrated a 16-channel, ∼26 bandwidth/channel, membrane DML array on $SiO_2$/Si capable of 1.6-Tbps [10]. However, in that demonstration, to achieve >100 Gbps per channel we had to rely on advanced PAM-4 modulation with reduced-complexity nonlinear equalization [13].

To further reduce system complexity and power consumption, membrane DML arrays that can achieve higher bandwidths and support symbol rates of 100 GBaud or more with simpler NRZ modulation are highly desirable. However, the intrinsic (i.e., carrier-photon) dynamics in DMLs impose limitations on the achievable bandwidth based on the relaxation oscillation frequency $(f_R)$, which, in turn, is proportional to the square-root of the operating bias current $(I_b)$ above threshold $(I_{th})$, $f_R \propto \sqrt{I_b - I_{th}}$, leading to an intrinsic power consumption - bandwidth tradeoff [11], [12]. To address this tradeoff, laser designs incorporating integrated optical feedback that take advantage of cavity and longitudinal modal effects [14], [15], [16], [17], [18], [19], [20], [21], [22], [23], notably the photon-photon resonance (PPR) effect, can be used to boost DML bandwidths by over 2 times without the need to increase the bias current. Using such PPR-enabled designs, we have previously demonstrated a record 108 GHz DML bandwidth over a membrane laser

Manuscript received 15 December 2023; revised 30 January 2024; accepted 13 February 2024. Date of publication 16 February 2024; date of current version 14 June 2024. *(Corresponding author: Nikolaos-Panteleimon Diamantopoulos.)*

Nikolaos-Panteleimon Diamantopoulos, Takuro Fujii, Hidetaka Nishi, Koji Takeda, Toru Segawa, and Shinji Matsuo are with the NTT Device Technology Labs, Nippon Telegraph and Telephone Corporation, Atsugi 243-0198, Japan (e-mail: np.diamantopoulos@ntt.com; takuro.fujii@ntt.com; hidetaka.nishi@ntt.com; koji.takeda@ntt.com; toru.segawa@ntt.com; shinji.matsuo@ntt.com).

Suguru Yamaoka was with the NTT Device Technology Labs, Nippon Telegraph and Telephone Corporation, Atsugi 243-0198, Japan. He is now with the NTT Access Network Service Systems Labs, Nippon Telegraph and Telephone Corporation, Yokosuka 239-0847, Japan (e-mail: suguru.yamaoka@ntt.com).

Color versions of one or more figures in this article are available at https://doi.org/10.1109/JLT.2024.3366532.

Digital Object Identifier 10.1109/JLT.2024.3366532

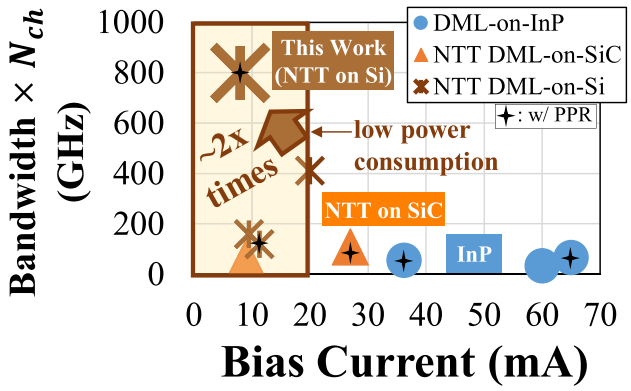


Fig. 1. Recent DML-Tx records: E-O bandwidth × no. of channels ($N_{ch}$).

fabricated on a high-thermal-conductivity SiC substrate [14] and a ~60 GHz, 2-channel membrane DML array on $SiO_2$/Si [12]. Moreover, record experiments have achieved unprecedented single-channel data rates exceeding 300 Gbps over a single DML, when advanced modulation, equalization, and RF signal generation techniques were used [24], [25]. Nevertheless, to date, there has not been a demonstration of a multi-channel DML array with more than two channels ($N_{ch}$> 2) that exhibits the PPR effect. This is partly attributed to the challenges in maintaining stable and controllable optical feedback for PPR across the entire array.

In this extended paper, we present the first multi-channel DML array with $N_{ch} > 2$, exhibiting stable PPR over 16 channels [26]. The membrane laser array demonstrated a bandwidth performance of ~50 GHz/channel, achieving the highest bandwidth × $N_{ch}$ product among all previous DML-Tx demonstrations (see Fig. 1) and more than 6.5× higher compared to all previous DML demonstrations exhibiting PPR. Moreover, the total Tx bandwidth was ~2× higher compared to our previous 16-channel membrane DML array demonstration [10]. Based on it, we have achieved 100 GBaud NRZ modulations over a short-reach link of 2 km in the O-band with <130 fJ/bit laser-operating energies, denoting a significant stride towards ultra-low power consumption Tx for next-generation 1.6 Tbps optical interconnects.

The paper is organized as follows. Following the introduction in Section I, the device structure, fabrication, and extended device characteristics are discussed in detail in Section II. Following that, Section III is focused on the experimental demonstration of the 100 GBaud NRZ signals over the short-reach 2-km link, while Section IV offers an updated and detailed discussion on the DML array design aspects for PPR optimization. Finally, a conclusion is provided in Section V.

## II. 16-Channel Membrane Laser Array With PPR

### A. Device Structure & Fabrication

The laser structure was based on our high grating coupling coefficient ($\kappa$) membrane structure on Si [5], [10], [11], [12]. As discussed in more details in Section IV, the high $\kappa$ of membrane lasers is very advantageous to achieve wide PPR control by allowing for the existence of several PPR regions within the available operating bias current range. In this work, we used an ultra-thin III-V membrane structure with a total III-V thickness of ~250 nm and a 6-period InGaAlAs multi-quantum well (MQW). This structure provided an even stronger optical confinement factor (between 16 ~ 18%) and a higher $\kappa$ (between 600 ~ 750 $cm^{-1}$) compared to our previous works on PPR lasers utilizing ~320-nm-thick III-V membranes [11], [12].

Distributed reflector (DR) lasers (shown schematically in Fig. 2(a)–(c)) composed of a middle 80-$\mu$m-long distributed feedback (DFB) section, a rear 80-$\mu$m-long distributed Bragg reflector (DBR-*r*) section, and a front 200-$\mu$m-long DBR (DBR-*f*) section, were fabricated based on a 16-channel, 1D arrayed layout (shown in Fig. 2(d)) with a 250-$\mu$m laser-to-laser pitch. The rear DBR-*r* was used for single-mode lasing with

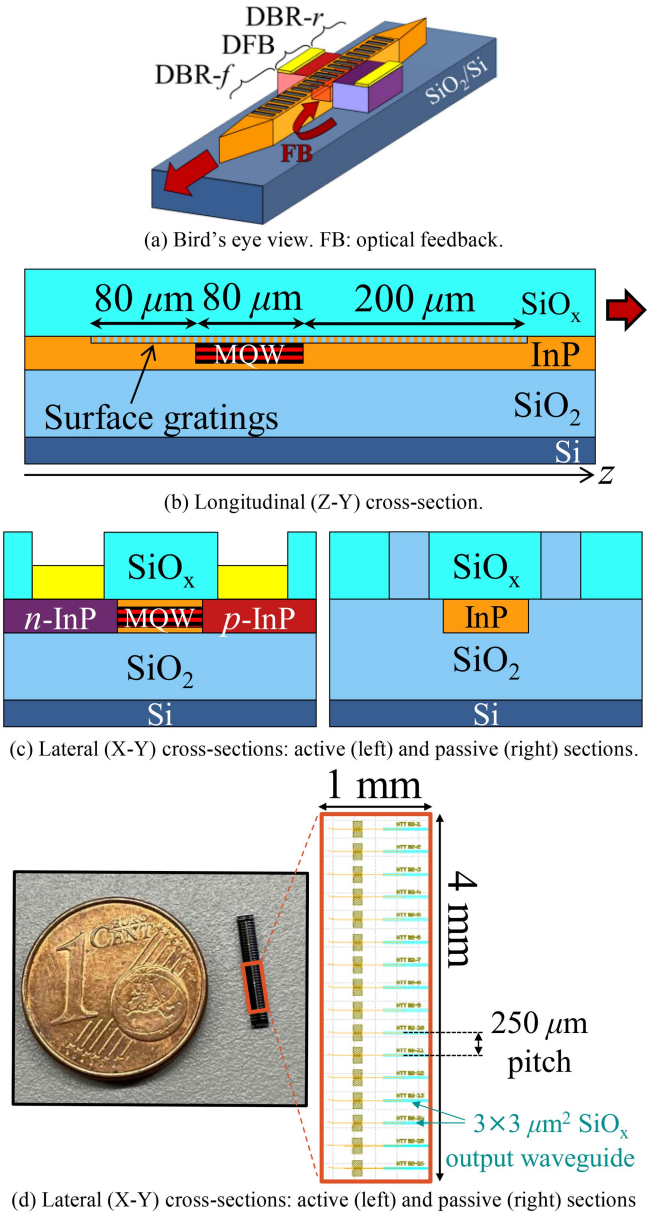


Fig. 2. Membrane DR laser array on $SiO_2$/Si with optical feedback.

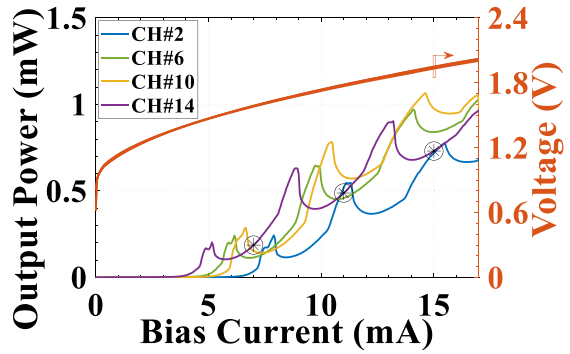


(a) Static L-I-V characteristics. Asterisks mark CH#14 points for (b), (c), (d).

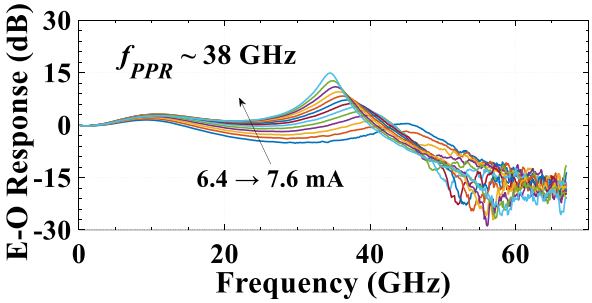


(b) E-O response at ~7 mA for CH#14.

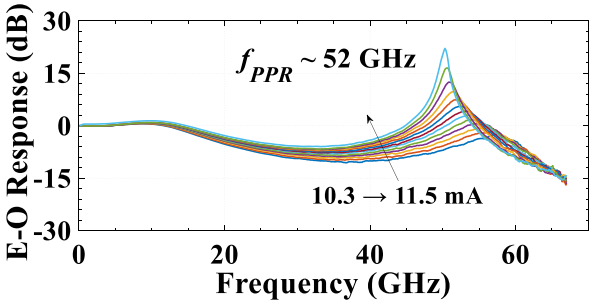


(c) E-O response at ~11 mA for CH#14.

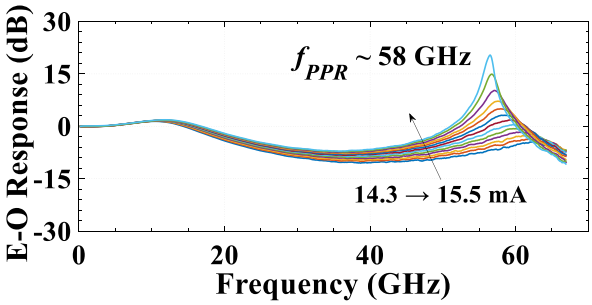


(d) E-O response at ~15 mA for CH#14.

Fig. 3. Static L-I-V and E-O responses for different PPR regions.

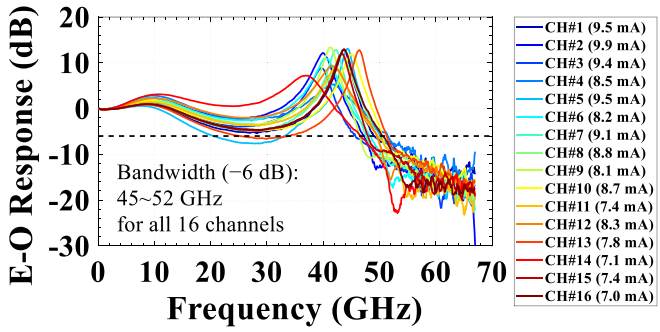


Fig. 4. E-O responses for all 16-channels (bias currents in parentheses were chosen based on bandwidth maximization).

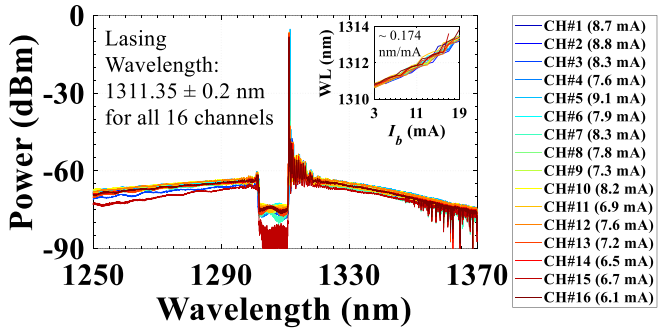


Fig. 5. Optical spectra for all 16-channels (bias currents in parentheses were chosen based on BER maximization results shown in Fig. 9). Insert: Lasing wavelength (WL) vs bias current ($I_b$).

reduced spatial and spectra hole-burning effects by filtering the longest wavelength mode of the two main longitudinal modes of the uniform DFB section, based on a Bragg wavelength detuning equal to around half of the DFB stopband width. The PPR, as well as the detuned-loading effects were produced by optical feedback generated by the long-wavelength side-lobes of the DBR-*f*, by having ~0-nm detuning between the DBR-*f* section and the DFB section [11], [12].

The device fabrication was based on our proprietary membrane III-V on Si heterogeneous integration technology and by using processes similar to other works presented by our group recently [10]. An epitaxially-grown III-V/InP wafer was directly bonded on a $SiO_2$/Si wafer and the lateral *p-i-n* laser array was fabricated by InP regrowth, Si-ion implantation (for *n*-InP) and Zn-diffusion (for *p*-InP), followed by a series of dry and wet etching processes. Since our device fabrication method using selective doping is the same as that of Si-CMOS, we believe that it is suitable for high volume production. Moreover, we used a buried heterostructure (BH) in which the active region is surrounded by a high thermal conductivity InP layer. This BH structure provides efficient carrier and optical confinement in the active region, while the InP layer also helps on removing the heat near the active region. Therefore, a high modulation efficiency can be achieved on $SiO_2$, with high-speed modulation and low power consumption. Surface InP gratings were formed by a UV lithography process with 0.25-nm resolution. This time, the designed $\kappa$ coefficients for the DFB and DBR sections were around 700 $cm^{-1}$. For direct edge coupling to ultra-high numerical aperture (UHNA) fibers, spot-size converters were integrated based on 3 × 3 $SiO_x$ waveguides and InP tapers [5]. Note that, no heaters were integrated as they were not necessary for the PPR control of the array (see detailed discussion in Section IV).

The total chip size (see photo inset in Fig. 2(c)) was 1 × 4 $mm^2$. In the future this can be further reduced to ~3 × 1 $mm^2$ (with no performance penalty) by utilizing the 2D, 16-channel DML layout presented in Ref. [10].

### B. Device Characteristics

Measured static L-I-V curves for four different channels are shown in Fig. 3(a). The output power here denotes fiber-coupled powers and the measurements were performed at a stage-controlled room temperature of 25 °C. The maximum fiber-coupled output power for all channels was between 0.75 $\sim$ 1.1 mW. For each of these curves, four super-linear regions are observed up to 17 mA of applied bias current. These super-linear L-I regions were generated by the filtering effect of DBR-*f*. Similarly to previous works [11], [12], [21], it is in these regions that the PPR effect is observed. Note that a fifth super-linear PPR region also exists for several channels for bias currents >17 mA (not shown here). The large number of available PPR regions is due to the higher $\kappa$ design, as explained in Section IV in more details.

Fig. 3(b)–(d) present measured E-O responses for the 2nd, 3rd, and 4th PPR regions for channel (CH) #14. As it can be seen from these figures, the PPR frequency ($f_{PPR}$) increases at higher bias currents, from ~38 GHz at ~7 mA to ~58 GHz at ~15 mA. A similar trend has been observed for all channels and with various previous devices. The existence of multiple $f_{PPR}$ within the same device as well as the trend they follow, allows for an inherent control mechanism via bias current tuning for maximizing the DML bandwidth, without any need to integrate, e.g., heaters for PPR control (see more details about this in Section IV).

In this work, we chose to work with the 2nd PPR region (between 6 $\sim$ 10 mA, $f_{PPR} \sim$ 40 GHz) for all 16 channels because this region maximized the E-O bandwidth while reducing the laser-operating power consumption (here, between 9.4 $\sim$ 15.7 mW per channel). However, future implementations shall be focused on larger bias current regions for achieving higher laser output powers.

The resulting E-O responses for all 16 channels at this PPR region are shown in Fig. 4. For this figure we took measurements using a bias current step of 0.1 nm and then plotted the E-O responses for the bias current that maximized the bandwidth of each channel. As it can be seen by this figure, the −6 dB down bandwidth was between 45 $\sim$ 52 GHz for all 16 channels. Note that, although a dip of several dBs appears between $f_{PPR}$ and $f_R$ for some channels, such non-uniformities in the E-O response can be mitigated by typical linear equalization employed in most transceivers. Although there is some deviation between the E-O responses among the 16 channels, we believe that this deviation is not significant for practical use (see detailed discussion about stability in Section IV-A). Also, note that a better E-O response matching for all 16 channels could have been achieved for smaller bias current steps, e.g., 0.01 mA.

Fig. 5 depicts the measured DC spectra for all 16 channels taken within the operating bias current regions that minimize the bit-error rate (BER) results discussed in Section III. Importantly, all 16 channels lased at around 1311.35 nm with a lasing wavelength deviation of only ±0.2 nm. This attests to the stability of the grating-based design, which is beneficial for multi-channel PPR control (as discussed in more details in Section IV). The side-mode suppression ratio of all channels remained >40 dB

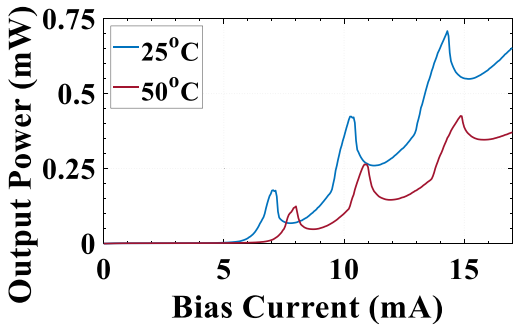


(a) Static L-I curves.

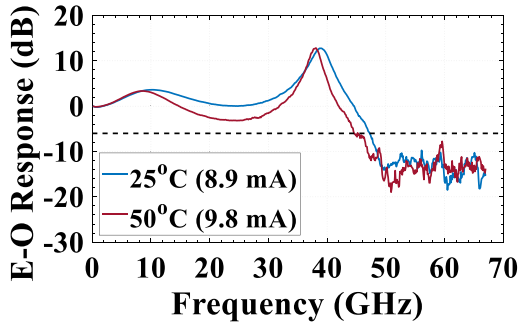


(b) E-O responses (bias currents in parentheses).

Fig. 6. Temperature dependance (CH#4 is shown here).

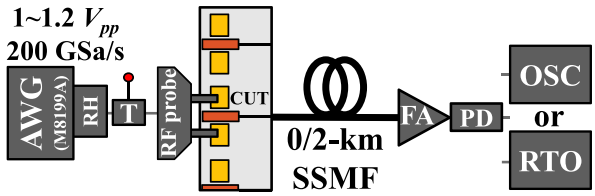


Fig. 7. Experimental setup. CUT: Channel under test; AWG: Arbitrary waveform generator; RH: Remote head of AWG; T: Bias tee; SSMF: Standard single-mode fiber; FA: Praseodymium-doped fiber amplifier; PD: Photodetector; OSC: Sampling oscilloscope; RTO: Real-time oscilloscope.

and the linear dependency of the lasing wavelength vs. bias current dependency was ~0.174 nm/mA on average for all channels (inset of Fig. 5).

Finally, regarding operating temperature dependancy, Fig. 6 depicts the L-I-V and E-O responses for CH#4 at 25 °C and 50 °C. These results show similar trends observed in our previous works [11], [12], where we had numerically and experimentally studied the PPR effect for this laser structure on $SiO_2$/Si for temperatures up to 75 °C. In particular, both $f_{PPR}$ and $f_R$ reduce at the higher 50 °C temperature, although, as expected (see Ref. [12]), the reduction of the $f_{PPR}$ is smaller than that of the $f_R$. This simultaneous reduction of both $f_{PPR}$ and $f_R$ maintains the PPR effect and a large E-O bandwidth with a small $f_{PPR}$-$f_R$ dip at such temperatures and provides a temperature tolerance for the overall bandwidth and PPR effect for the entire array. Note that, based on the previous results obtained in Ref. [12], this time, we focus only on semi-cool operating temperatures up to 50 °C for this PPR laser structure on $SiO_2$/Si. Regarding uncooled operation of DML even up to 85 °C, our focus remains on our PPR membrane DMLs on high-thermal-conductivity SiC substrates [15].

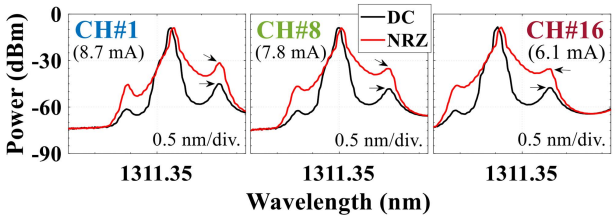


(a) DC vs. 100 GBaud NRZ modulated spectra. The black arrows indicate at PPR side-modes used.

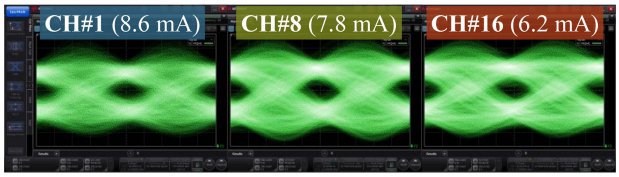


(b) Eye diagrams obtained by a sampling oscilloscope at back-to-back.

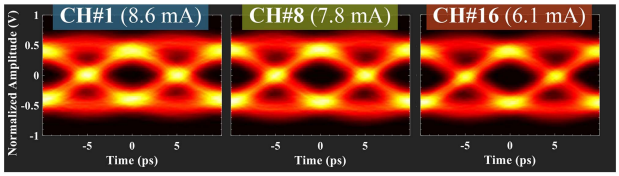


(c) Eye diagrams obtained after 2-km transmissions after offline processing.

Fig. 8. Measured characteristics for 100 GBaud NRZ modulated signals.

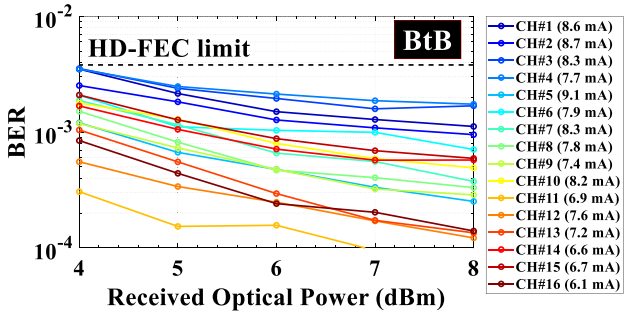


(a) Back-to-back (BTB).

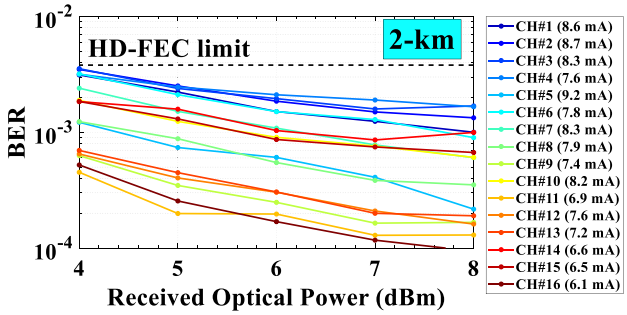


(b) After 2-km transmission.

Fig. 9. Bit-error rate (BER) vs. received optical power (ROP).

## III. Experimental Demonstration: 2-km Link

The experimental setup used for the 100-GBaud NRZ measurements is shown in Fig. 7. The NRZ signals were generated by an arbitrary waveform generator (AWG model: Keysight M8199A) at 200 GSa/s and a peak-to-peak voltage, $V_{pp} = 1{\sim}1.2$ V. The chip was driven by a 67-GHz-bandwidth RF probe and bias-tee via a short (<30 cm) RF cable. The output of each channel under test (CUT) was butt-coupled to a UHNA which was thermally-expansion core (TEC)-spliced to a standard single-mode fiber (SSMF) pigtail. At the receiver side, a praseodymium-doped fiber amplifier (FA) was used for reaching the optimum (around +8 dBm) input power to a commercial 70G *p-i-n* photodetector (without trans-impedance amplifier) for detection. Note that, as in our previous works [11], [12], such optical amplification is not required if we further increase the output power by optimizing the grating coupling coefficient and selecting a higher PPR region. Finally, the signals were detected by a conventional sampling oscilloscope (OSC) or by a 63-GHz-bandwidth, 160-GSa/s real-time oscilloscope (RTO) for BER measurements. In both cases a 21-tap linear feed-forward equalizer was used (OSC: build-in function with T-spaced taps, RTO: offline processing with T/2-spaced taps). Other measurement equipment, not shown in Fig. 7, included a 95:5 optical coupler for received optical power (ROP) monitoring and an optical spectrum analyzer for spectrum measurements.

Fig. 8 presents measured spectra and eye diagrams for the 100 GBaud NRZ signal modulations for CH#1, CH#8, and CH#16. The PPR effect can be clearly seen by the enhancement of the high-frequency signal components in the modulated spectra in Fig. 8(a). Moreover, clear eye openings could be observed for all channels (Fig. 8(b) and (c)) for the 100 GBaud NRZ signals at ROP = +7 dBm, with better eye openings obtained by the offline processing due to the better performance of the linear equalizer used.

Finally, Fig. 9 summarizes the BER versus ROP performances for all 16 channels at optical back-to-back (BtB) and after 2-km SSMF transmissions. All channels could achieve a BER below the 6.69%-overhead hard-decision forward-error correction (HD-FEC) threshold [27] at ROPs $\geq$ +4 dBm. Based on the operating bias currents for the 2-km transmissions shown in the legend of Fig. 9 and the corresponding measured bias voltages (see I-V curves in Fig. 3(a)), a total of ~126 fJ/bit laser-array-operating energy was achieved for the entire 16-channel DML array.

## IV. Design Considerations For PPR Control

### A. Comparison of PPR Designs & PPR Stability

For achieving a stable multi-channel DML array exhibiting the PPR effect, longitudinal mode stability and controllability are essential. Typical coupled-cavity laser designs with integrated optical feedback that enable the PPR effect can be mostly categorized into two types (Fig. 10): (i) laser diodes integrated with a passive waveguide and a front mirror (WG+R) [14], [15], [18], [22] or (ii) DR laser designs with DBR-based feedback [11], [12], [17], [21].

Although laser designs based on WG+R are simple to design and fabricate, it could be challenging to achieve a controlled $f_{PPR}$ for all channels in a DML array. This is because the phase and reflectivity of the optical feedback could widely vary within the laser array depending on the processes involved in the fabrication of the mirror R. This is illustrated in the schematic

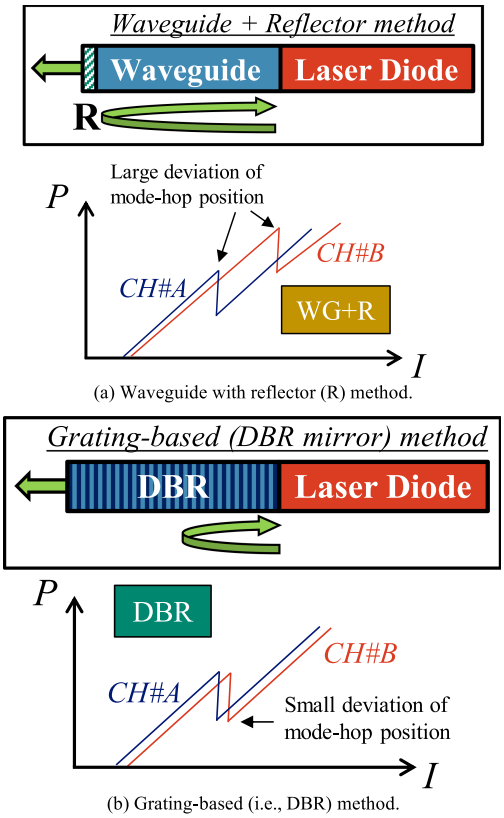


(a) Waveguide with reflector (R) method.

(b) Grating-based (i.e., DBR) method.

Fig. 10. Integrated optical feedback methods for PPR.

of Fig. 10(a), which depicts a large deviation of the mode-hop position, which typically follows the usable PPR region.

On the other hand, DBR-based feedback lasers fabricated with mature epitaxy processes can achieve stable PPR control over large arrays. This is because of the high Bragg wavelength accuracy and yield offered by modern high-resolution lithography tools. This is illustrated in the schematic of Fig. 10(b), where in this case the deviation of the mode-hop position within a laser array is minimized. Moreover, DBRs can also be used as front mirrors instead of conventional R mirror in a hybrid WG+DBR approach [23], which could simplify the design further.

In this work, (by considering all experimental results, including the L-I curves in Fig. 3(a), the E-O responses in Fig. 4, the DC spectra in Fig. 5, and the BER results in Fig. 9) the bias current deviation for PPR and mode-hopping was within $\pm$1.55 mA. We believe that this bias current deviation is not significant and can be handled by conventional bias current control circuits for, e.g., volume production, avoiding, thus, integration of additional active elements such as heaters for PPR feedback control which would increase the power consumption. The bias current deviation resulted in a wavelength deviation of $\pm$0.2 nm (Fig. 9), which was within the limits of the resolution of the lithography tool used to form the gratings in the current device (0.25-nm resolution, corresponding to a Bragg wavelength resolution of $\sim$1 nm). In the future, we could utilize higher resolution lithography tools (currently available at our labs), aiming at demonstrating even better PPR stability and yield.

Lastly, focusing more on membrane lasers on Si, the requirements for $f_{PPR}$ are more stringent than previous approaches that relied on WG+R methods, i.e., lasers on InP or membrane lasers on SiC [14], [15], [18], [22]. This is because the $f_R$ of membrane lasers on Si is typically $\leq$20 GHz [5], [10], which means that $f_{PPR}$ needs to be quite small, i.e., between 30 $\sim$ 60 GHz, for reducing the $f_{PPR}$-$f_R$ dip and, hence, achieving a flat E-O response for modulation bandwidth maximization. Having several such small $f_{PPR}$ values within the available bias current range (typically 10 $\sim$ 20 mA or so for membrane lasers on Si) ar e hard to obtain using the WG+R method since the free-spectral range of the resulting Fabry-Pérot filtering is inversely proportional to the WG length, and long WG lengths are therefore necessary. This often leads to high losses and/or single-mode lasing instabilities. (On the other hand, the required $f_{PPR}$ of $\sim$90 GHz for membrane laser on SiC can be achieved using an InP waveguide with a length of less than 150 $\mu$m, resulting in a 250$\sim$300 GHz free-spectral range [14], [15]). However, this problem is solved with the DBR method since the spacing and the reflectivity of the DBR side-lobes can be designed by the $\kappa$ and DBR length, which is shorter than the WG length in the WG+R case.

### B. Dependency of PPR Frequency on Bias Current

A critical issue that needs further clarification is the dependency of $f_{PPR}$ on the applied bias current. A stable $f_{PPR}$ will allow for a simplification on the design and control, while a predictable $f_{PPR}$ dependency on the bias current allows for another degree of freedom in bandwidth control which is particularly useful in the case of multi-channel arrays.

As the experimental results in Fig. 3 highlight, it appears that the $f_{PPR}$ increases by increasing the bias current. Similar trend was observed not only in all other channels in the present array, but also in previously fabricated devices [11], [12], including devices based on the WG+R method [14], [15]. In particular, the persistent appearance of this trend even in the WG+R case (in which all side-modes experience a similar reflectance and phase from R, unlike in the DBR case), signifies that this is a universal trend of high importance.

One way to explain this trend is extending upon the analysis we presented previously on the dependance of $f_{PPR}$ on the operating temperature [12]. In our previous work [12], we showed that the reduction of $f_{PPR}$ at higher temperatures is attributed to the reduction of the gain, which further leads to a lower power for the side-modes. Conversely, the opposite is true in the case of increasing bias current: by increasing the bias current, the gain experienced by the side-modes increases, leading them to have higher powers. Since the appearance of the PPR effect on the E-O response effectively depends on the PPR side-mode suppression ratio ($SMSR_{PPR}$) between the main lasing mode and the PPR side-mode, changes on the gain/power of PPR side-modes due to temperature and bias current changes, would directly affect it. Moreover, considering a frequency domain analysis depending on the phase, it can be understood that the thermal (i.e., self-heating) chirp, $f_T$, and the carrier (i.e., bias current-dependent) chirp, $f_N$, will, respectively,

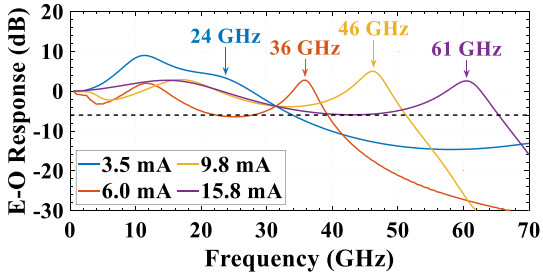


(a) Simulated E-O responses for different PPR regions.

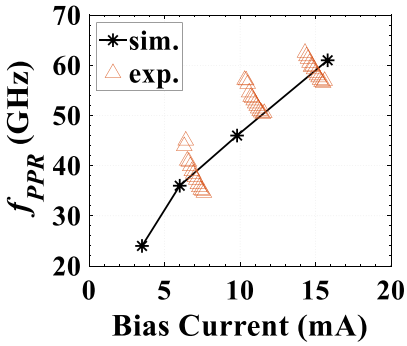


(b) PPR frequency ($f_{PPR}$) vs. bias current.

Fig. 11. PPR frequency for different PPR regions.

red-shift or blue-shift the wavelength of the main lasing mode through changes of the effective index of the gain section. This effectively translates to a smaller (see also Ref. [22]) or larger $f_{PPR}$, respectively. Since $f_N$ is proportional to the gain term $a_H \Gamma \frac{\partial g}{\partial N} \Delta N$ [28], with $a_H$ denoting the linewidth enhancement factor, $\Gamma$ denoting the confinement factor, $\frac{\partial g}{\partial N}$ denoting the differential gain, and $\Delta N$ denoting the carrier density increase (i.e., from the threshold value), this analysis provides another avenue for explaining the $f_{PPR}$ dependency on the bias current and gain.

Moreover, another factor that affects the $f_{PPR}$ relationship with the bias current is the longitudinal structure. As shown by the modal calculations in Fig. 12(b) (more discussions about the modal analysis follows in the next sub-section), drawn here using $a_H = 0$for our DBR-based feedback structure, PPR regions at larger bias currents have larger $f_{PPR}$. We believe that this is due to the different phases for the different side-lobes (also note that, side-lobe spacing and bandwidth increases at longer wavelengths) and should not be prominent in structures in which the feedback modes have negligible/small wavelength dependencies (e.g., Fabry-Pérot modes in WG+R case).

To confirm all the above, we performed simulations using an in-house developed laser simulator based on the travelling-wave model [11], [29], capable of simulating complex modal dynamics and longitudinal effects. The resulting E-O responses for our structure at different bias currents are shown in Fig. 11(a). Here, $\kappa$ was set equal to 600 $cm^{-1}$ for the DBR sections and $a_H$ was set equal to 3 based on previous measurements [11]. As it can be seen, the trend of increasing $f_{PPR}$ at higher bias currents can be seen. Moreover, when this trend is plot in comparison to the experimental results for $f_{PPR}$ from Fig. 3, the trend between simulations and experiments is within very

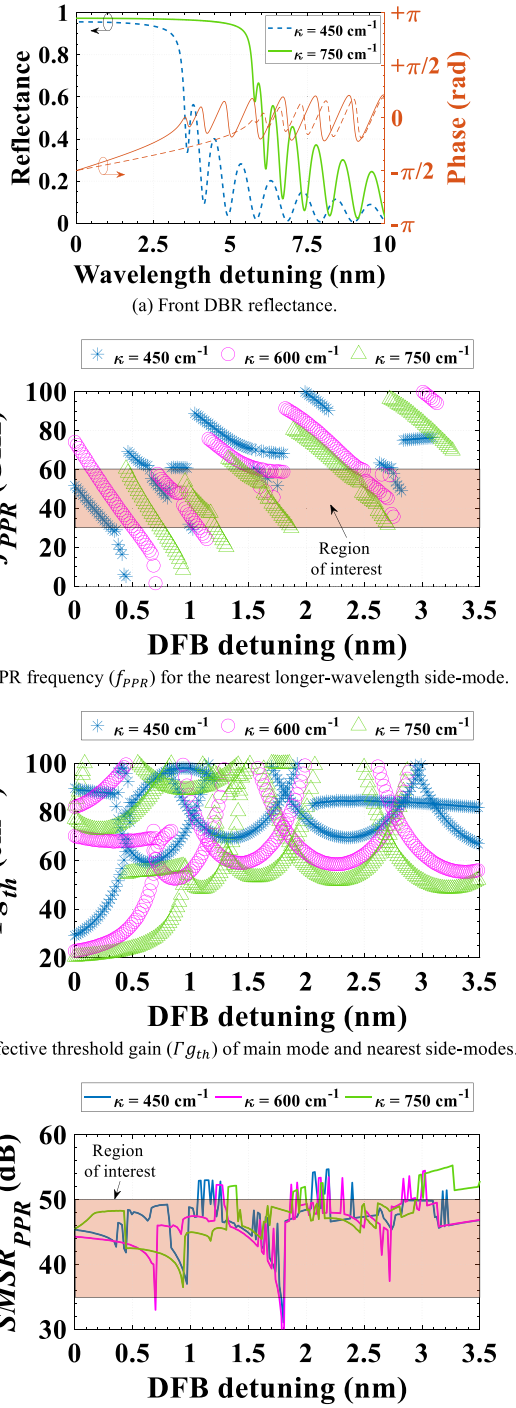


(a) Front DBR reflectance.

(b) PPR frequency ($f_{PPR}$) for the nearest longer-wavelength side-mode.

(c) Effective threshold gain ($\Gamma g_{th}$) of main mode and nearest side-modes.

(d) Side-mode suppression ratio ($SMSR_{PPR}$) between the main lasing mode and the nearest longer-wavelength side-mode accounting for the PPR effect.

Fig. 12. Design optimization based for different coupling coefficients ($\kappa$).

good agreement (Fig. 11(b)). Note that the decrease of $f_{PPR}$ within each PPR region (shown here for the experimental results, but also confirmed in simulations) is due to the self-heating effect [22]. Such analysis can benefit future designs by further optimizing and controlling $f_{PPR}$ and bias currents in DML arrays. Moreover, by selecting an appropriate bias current and PPR region as we have done with the current DML array, there is no need for heater integration for PPR control.

### C. Grating Design Optimization

Our DBR-based DR laser structure for PPR takes advantage of the high $\kappa$ of the membrane structure. Compared to our previous works on PPR for membrane lasers on Si [11], [12], this time we have further increased the $\kappa$ of our membrane lasers on Si from previously 400 $\sim$ 480 cm$^{-1}$ to 600 $\sim$ 730 cm$^{-1}$ in this work. As it can be seen by the simulated DBR reflectance spectra in Fig. 12(a), such higher $\kappa$ increases the reflectivity and decreases the spacing of DBR side-lobes, meaning that more side-modes and PPR regions are expected to appear within the available bias current range, hence, increasing the chances of achieving a suitable PPR regime for all 16 channels. This has been confirmed by comparing the L-I curves in Fig. 3(a) with those in Refs. [11], [12], where the super-linear regions appear closer together in the former compared to the latter.

The impact of different $\kappa$ values in the PPR effect, is depicted by the modal analysis results shown in Fig. 12(b)–(d). Here, the $x$-axis denotes detuning of the DFB Bragg wavelength (e.g., due to self-heating). Note that, the DFB detuning range between 0 $\sim$ 3.5 nm is typical for our membrane lasers on Si, considering the available bias current range. Fig. 12(b) depicts the $f_{PPR}$ values between the main lasing mode and the nearest longer-wavelength side-mode. Focusing on the $f_{PPR}$ region of interest, i.e., between 30 $\sim$ 60 GHz, it can be observed that more PPR regions exist for higher $\kappa$ values of 600 $\sim$ 750 cm$^{-1}$ when compared to the $\kappa = 450$ cm$^{-1}$ case, which is close to the value used in our previous works [11], [12].

Finally, Fig. 12(c) and (d) depict the threshold gain ($g_{th,m}$) and estimated $SMSR_{PPR}$ values for our structure. The latter is related to $g_{th,m}$ via the threshold gain margin $\Delta g_{th,PPR} = g_{th,1} - g_{th,0}$ between the main lasing mode ($m = 0$) and the first PPR side-mode ($m = 1$) as follows:

$$SMSR_{PPR} \approx 10\log_{10}\left(1 - \frac{\Delta g_{th,PPR}}{g - g_{th,0}} \frac{\Gamma g - a_i}{\Gamma g_{th,1} - a_i}\right). \quad (1)$$

Here, (1) was derived from (3.81) in Ref. [28], assuming that lasing mostly occurs from the front facet due to high back-mirror reflectivity from DBR-$r$ (i.e., $F_{1,0} \approx F_{1,1} \approx 1$) and that the two modes experience similar modal gains ($g \equiv g_0 \approx g_1$), insertion losses ($a_i$), and confinement factors ($\Gamma$). Moreover, based on various experimental spectra on PPR lasers, including those obtained from previous devices (see Fig. 8(a) as well as results in Refs. [11], [12]), we have observed that a good $SMSR_{PPR}$ value for appropriate PPR effect and single-mode lasing is between 35 $\sim$ 50 dB, with the current higher-$\kappa$ devices denoting $\sim$5 dB lower $SMSR_{PPR}$ values compared to previous ones [11], [12]. Considering $\Gamma\Delta g_{th,PPR}$ values up to 150 cm$^{-1}$, derived by the modal $g_{th,m}$ values in Fig. 12(c), similar $SMSR_{PPR}$ ranges (Fig. 12(d)) can be obtained when plotted for gain values of $g = 99.999\% \times g_{th,0}$, which satisfies well the necessary lasing condition $g \cong g_{th,0}$ at PPR regions.

Future works shall focus on further optimizing the array structure to increase the output power and utilize a higher PPR region.

## V. Conclusion

To meet the increasing demand for higher data rates and lower power consumption transceivers for data center networks and CPO we have demonstrated the first 16-channel directly modulated laser array exhibiting the PPR effect. Bandwidths of $\sim$50 GHz at bias currents between 6.1 $\sim$ 9.2 mA have been achieved for all 16 channels in a membrane laser array on $SiO_2$/Si with optimized integrated optical feedback for stable PPR control, denoting a record bandwidth $\times$ $N_{ch}$ product. Moreover, the DML array has been demonstrated in a short-reach 2-km link in the O-band by using 100-GBaud NRZ modulations. BERs below an HD-FEC limit were achieved, resulting in $<$130 fJ/bit laser-operating energies. Also, our membrane DMLs on $SiO_2$/Si can be natively integrated with membrane PD arrays on $SiO_2$/Si [30] and passive Si(N) filters to form complete membrane transceiver modules. These results denote a significant stride for the use of directly modulated membrane lasers towards ultra-low power consumption transmitters for 1.6 Tbps interconnects and beyond.

## Acknowledgment

The authors would like to acknowledge our process technicians Y. Shoji and Y. Yokoyama for support with device fabrications and our testing technician S. Hirata for support with measurements.

## References

[1] "Global cloud index: Forecast and methodology 2016-2021," Cisco, 2018. [Online]. Available: https://virtualization.network/Resources/Whitepapers/0b75cf2e-0c53-4891-918e-b542a5d364c5_white-paper-c11-738085.pdf

[2] "2023 ethernet roadmap," Ethernet Alliance, 2023. [Online]. Available: https://ethernetalliance.org/technology/ethernet-roadmap/

[3] "Optical connectivity options for 400 Gbps and higher on-board optics," Consortium for on-board optics (COBO), Nov. 2019. [Online]. Available: https://www.onboardoptics.org/race-to-800g-a-reality-check-micros-1

[4] S. Matsuo and T. Kakitsuka, "Low-operating-energy directly modulated lasers for short-distance optical interconnects," *Adv. Opt. Photon.*, vol. 10, no. 3, pp. 567–643, Sep. 2018, doi: 10.1364/AOP.10.000567.

[5] H. Nishi et al., "Membrane distributed-reflector laser integrated with $SiO_x$-based spot-size converter on Si substrate," *Opt. Exp.*, vol. 24, no. 16, pp. 18346–18352, Aug. 2016, doi: 10.1364/OE.24.018346.

[6] T. Fujii et al., "Multiwavelength membrane laser array using selective area growth on directly bonded InP on $SiO_2$/Si," *Optica*, vol. 7, no. 7, pp. 838–846, Jul. 2020, doi: 10.1364/OPTICA.391700.

[7] H. Nishi et al., "Integration of eight-channel directly modulated membrane-laser array and SiN AWG multiplexer on Si," *J. Lightw. Technol.*, vol. 37, no. 2, pp. 266–273, Jan. 2019, doi: 10.1109/JLT.2018.2873742.

[8] N.-P. Diamantopoulos et al., "400-Gb/s DMT-SDM transmission based on membrane DML-array-on-silicon," *J. Lightw. Technol.*, vol. 37, no. 8, pp. 1805–1812, Apr. 2019, doi: 10.1109/JLT.2018.2885792.

[9] N.-P. Diamantopoulos, T. Fujii, H. Nishi, K. Takeda, T. Segawa, and S. Matsuo, "Energy-efficient 500/800 Gbps short-reach SDM interconnects based on directly-modulated membrane lasers on silicon," in *Proc. Eur. Conf. Opt. Commun.*, 2023, Paper P5.

[10] T. Fujii et al., "16-channel membrane directly modulated laser array on Si for 2-km transmission of 112-Gbps PAM-4," in *Proc. Eur. Conf. Opt. Commun.*, 2023, Paper We.B.4.1.

[11] N.-P. Diamantopoulos et al., "47.5 GHz membrane-III-V-on-Si directly modulated laser for Sub-pJ/bit 100-Gbps transmission," *Photonics*, vol. 8, no. 2, Jan. 2021, Art. no. 31, doi: 10.3390/photonics8020031.

[12] N.-P. Diamantopoulos et al., "60 GHz bandwidth directly modulated membrane III-V lasers on $SiO_2$/Si," *J. Lightw. Technol.*, vol. 40, no. 10, pp. 3299–3306, May 2022, doi: 10.1109/JLT.2022.3153648.

[13] N.-P. Diamantopoulos, H. Nishi, W. Kobayashi, K. Takeda, T. Kakitsuka, and S. Matsuo, "On the complexity reduction of the second-order Volterra nonlinear equalizer for IM/DD systems," *J. Lightw. Technol.*, vol. 37, no. 4, pp. 1214–1224, Feb. 2019, doi: 10.1109/JLT.2018.2890118.
[14] S. Yamaoka et al., "Directly modulated membrane lasers with 108 GHz bandwidth on a high-thermal-conductivity silicon carbide substrate," *Nature Photon.*, vol. 15, no. 1, pp. 28–35, Jan. 2021, doi: 10.1038/s41566-020-00700-y.
[15] S. Yamaoka et al., "Uncooled 100-GBaud directly modulated membrane lasers on SiC substrate," *J. Lightw. Technol.*, vol. 41, no. 11, pp. 3389–3396, Jun. 2023, doi: 10.1109/JLT.2023.3239614.
[16] U. Feiste, "Optimization of modulation bandwidth in DBR lasers with detuned Bragg reflectors," *IEEE J. Quantum Electron.*, vol. 34, no. 12, pp. 2371–2379, Dec. 1998, doi: 10.1109/3.736110.
[17] G. Morthier, R. Schatz, and O. Kjebon, "Extended modulation bandwidth of DBR and external cavity lasers by utilizing a cavity resonance for equalization," *IEEE J. Quantum Electron.*, vol. 36, no. 12, pp. 1468–1475, Dec. 2000, doi: 10.1109/3.892568.
[18] M. Radziunas et al., "Improving the modulation bandwidth in semiconductor lasers by passive feedback," *IEEE J. Sel. Topics Quantum Electron.*, vol. 13, no. 1, pp. 136–142, Jan./Feb. 2007, doi: 10.1109/JSTQE.2006.885332.
[19] H. Dalir and F. Koyama, "Bandwidth enhancement of single-mode VCSEL with lateral optical feedback of slow light," *IEICE Electron. Exp.*, vol. 8, no. 13, pp. 1075–1081, Jul. 2011, doi: 10.1587/elex.8.1075.
[20] A. Abbasi et al., "Direct and Electroabsorption modulation of a III-V-on-silicon DFB laser at 56 Gb/s," *IEEE J. Sel. Topics Quantum Electron.*, vol. 23, no. 6, Nov./Dec. 2017, Art. no. 1501307, doi: 10.1109/JSTQE.2017.2708606.
[21] Y. Matsui et al., "55 GHz bandwidth distributed reflector laser," *J. Lightw. Technol.*, vol. 35, no. 3, pp. 397–403, Feb. 2017, doi: 10.1109/JLT.2017.2650678.
[22] Y. Matsui, R. Schatz, D. Che, F. Khan, M. Kwakernaak, and T. Sudo, "Low-chirp isolator-free 65-GHz-bandwidth directly modulated lasers," *Nature Photon.*, vol. 15, no. 1, pp. 59–63, Jan. 2021, doi: 10.1038/s41566-020-00742-2.
[23] K. Nishimura et al., "Direct modulation of membrane DR laser involving photon-photon resonance by 5G mobile signal in millimeter-wave band," in *Proc. Opto-Electron. Commun. Conf.*, 2023, Paper OECC2023-0320-24, doi: 10.1109/OECC56963.2023.10209954.
[24] D. Che, Y. Matsui, X. Chen, R. Schatz, and P. Iannone, "400-Gb/s direct modulation using a DFB+R laser," *Opt. Lett.*, vol. 45, no. 12, pp. 3337–3339, Jun. 2020, doi: 10.1364/OL.392873.
[25] N.-P. Diamantopoulos et al., "$>$100-GHz bandwidth directly-modulated lasers and adaptive entropy loading for energy-efficient $>$300-Gbps/$\lambda$ IM/DD systems," *J. Lightw. Technol.*, vol. 39, no. 3, pp. 771–778, Feb. 2021, doi: 10.1109/JLT.2020.3021727.
[26] N.-P. Diamantopoulos et al., "16-channel directly-modulated membrane laser array on Si utilizing photon-photon resonance for 1.6 Tbps interconnects," in *Proc. Eur. Conf. Opt. Commun.*, 2023, Paper Th.C.1.6.
[27] *Forward Error Correction for High Bit-Rate DWDM Submarine Systems*, ITU-T Recommendation G.975.1, Appendix I.9, 2004. [Online]. Available: https://www.itu.int/rec/T-REC-G.975.1-200402-I/en
[28] L. A. Coldren, S. W. Corzine, and M. L. Mašanović, *Diode Lasers and Photonic Integrated Circuits*, 2nd ed. Hoboken, NJ, USA: Wiley, 2012.
[29] B.-S. Kim, Y. Chung, and J.-S. Lee, "An efficient split-step time-domain dynamic modeling of DFB/DBR laser diodes," *IEEE J. Quantum Electron.*, vol. 36, no. 7, pp. 787–794, Jul. 2000, doi: 10.1109/3.848349.
[30] H. Nishi et al., "Integrated PAM-4 WDM receiver by InGaAsP-based membrane PDs and SiN demultiplexer on Si," in *Proc. IEEE Photon. Conf.*, 2019, Paper MD1.1, doi: 10.1109/IPCon.2019.8908477.

**Nikolaos-Panteleimon (Pandelis) Diamantopoulos** (Senior Member, IEEE) was born in Athens, Greece in 1988. He received the B.Sc. degree from the University of Peloponnese, Tripoli, Greece in 2009, the double M.Sc. degrees from Aston University, Birmingham, U.K., and Scuola Superiore Sant'Anna, Pisa, Italy, in 2012, under the joint-masters Erasmus Mundus E.U. Program, and the Ph.D. degree from Osaka University, Osaka, Japan, in 2016. Between 2011 and 2016, he was engaged with E.U.-funded R&D Projects with the Athens Information Technology Research Center, Athens, Greece. Since 2016, he has been with NTT Device Technology Labs, Atsugi, Japan. His research interests include ultra-high-speed semiconductor laser systems for communications and computing, integrated photonics, signal processing, optical communications, and neuromorphic photonics. Dr. Diamantopoulos is a Senior Member of OPTICA.

**Takuro Fujii** (Member, IEEE) was born in Kyoto, Japan, in 1986. He received the B.E. and M.E. degrees in system design engineering from Keio University, Tokyo, Japan, in 2010 and 2012, respectively. In 2012, he joined NTT Photonics Laboratories, Atsugi, Japan. He has been researching MOVPE growth of III-V semiconductors and the development of III-V semiconductor lasers on Si for photonic integrated circuits. Mr. Fujii is a Member of IEICE and JSAP. He was the recipient of the Young Scientist Presentation Award from JSAP in 2014.

**Suguru Yamaoka** was born in Osaka, Japan, in 1993. He received the B.E., M.E., and Ph.D. degrees in applied physics from Osaka City University, Osaka, Japan, in 2015, 2017, and 2021, respectively. In 2017, he joined NTT Device Technology Labs, Atsugi, Japan. His research interests include high-speed and low-power-consumption directly modulated semiconductor lasers. Dr. Yamaoka is a Member of IEICE and JSAP.

**Hidetaka Nishi** (Member, IEEE) received the B.S. and M.S. degrees in mechanical science and engineering and the Ph.D. degree in electronics and applied physics from the Tokyo Institute of Technology, Tokyo, Japan, in 2005, 2007, and 2016, respectively. In 2007, he joined NTT Microsystem Integration Laboratories. Since then, he has been conducting research on integrated photonic and plasmonic devices. Dr. Nishi is a Member of OPTICA and JSAP.

**Koji Takeda** (Senior Member, IEEE) received the B.S., M.S., and Ph.D. degrees in electronics engineering from the University of Tokyo, Tokyo, Japan, in 2005, 2007, and 2010, respectively. From 2008 to 2010, he received a research fellowship for young scientists from the Japan Society for the Promotion of Science. In 2010, he joined NTT Photonics Laboratories. His research interests include ultralow-power optical interconnects, InP photonic integrated circuits, and photonic crystal lasers. Dr. Takeda is a Member of IEICE and JSAP. He was the recipient of the Best Student Paper Award from the IEEE Photonics Society in 2009 and Outstanding Student Presentation Award from JSAP in 2010.

**Toru Segawa** (Member, IEEE) received the B.E. and M.E. degrees in electrical engineering and the Ph.D. degree in integrated design engineering from Keio University, Yokohama, Japan, in 1999, 2001, and 2012, respectively. In 2001, he joined NTT Photonics Laboratories, Atsugi, Japan, and has been engaged in research on high-speed tunable lasers and optical switches monolithically integrated on InP substrates. He is currently with the NTT Device Technology Labs, Atsugi, Japan. Dr. Segawa is a Member of JSAP and IEICE.

**Shinji Matsuo** (Fellow IEEE) received the B.E. and M.E. degrees in electrical engineering from Hiroshima University, Hiroshima, Japan, in 1986 and 1988, respectively, and the Ph.D. degree in electronics and applied physics from the Tokyo Institute of Technology, Tokyo, Japan, in 2008. In 1988, he joined NTT Optoelectronics Laboratories, where he researched photonic functional devices using multiple quantum well pin modulators and VCSELs. In 1997, he researched optical networks using WDM technologies with NTT Network Innovation Laboratories. Since 2000, he has been researching lasers and heterogeneous integration of III-V and Si photonics devices with NTT Photonics Laboratories, Atsugi, Japan and NTT Device Technology Laboratories, Atsugi, Japan. Dr. Matsuo is a Member of the JSAP and IEICE and a Fellow of OPTICA.